









# Revisiting Electronic and Nuclear Sputtering from Ions at Mercury Using Linear Cascade Theory

Orenthal J. Tucker<sup>1,2</sup> , Liam S. Morrissey<sup>3,4</sup> , Rosemary M. Killen<sup>1</sup> , Matthew H. Burger<sup>5</sup> , Ronald J. Vervack Jr.<sup>6</sup> , and Daniel W. Savin<sup>7</sup> 

<sup>1</sup> NASA Goddard Space Flight Center, Greenbelt, MD 20771, USA; [orenthal.tucker@hamptonu.edu](mailto:orenthal.tucker@hamptonu.edu)

<sup>2</sup> Atmospheric and Planetary Sciences, Hampton University, 154 William R. Harvey Way, Hampton, VA 23668, USA

<sup>3</sup> Faculty of Engineering, Memorial University, St. John's, NL, Canada

<sup>4</sup> American Museum of Natural History, New York, NY 10024, USA

<sup>5</sup> Space Telescope Science Institute, 3700 San Martin Drive, Baltimore, MD 21218, USA

<sup>6</sup> Johns Hopkins Applied Physics Laboratory, 11100 Johns Hopkins Road, Laurel, MD 20723, USA

<sup>7</sup> Columbia Astrophysics Laboratory, Columbia University, 538 West 120th Street, New York, NY 10027, USA

Received 2025 April 11; revised 2025 September 18; accepted 2025 October 1; published 2025 November 12

## Abstract

This study revisits calculations using linear cascade theory (LCT) to estimate the relative importance of the ion-induced collisional sputtering yield (also referred to as knock-on, nuclear, or kinetic sputtering) and the ion-induced electronic sputtering yield. We focus on sputtering of Na from Mercury's surface using data from the Mercury Surface, Space Environment, Geochemistry and Ranging (MESSENGER) mission. The updated nuclear and electronic sputtering yields for H and He solar wind ions at 1 keV amu<sup>-1</sup>, respectively, are approximately an order of magnitude larger than the values calculated using LCT in M. A. McGrath et al. Compared to this earlier work, our study uses a factor of 10 larger Na surface fraction and a factor of 3 lower total atom surface density based on MESSENGER data that were not available when the McGrath et al. study was carried out. Additional differences are the use of new data more relevant to Mercury's surface minerals for the nuclear and electronic stopping-power cross sections and the surface binding energies. For the conditions considered in this study, the nuclear sputtering yields calculated using LCT show good agreement with the values calculated using recent binary collision approximation models. We qualitatively compare estimates of the Na sputtering source rate to other source processes for Mercury's exosphere, considering recent studies of the precipitating ion flux based on MESSENGER data. Future experiments that measure the yield and ejecta energy spectra for simulated Mercury surface conditions, along with advanced modeling of ion-surface interactions, are required to reduce uncertainties and support exospheric studies.

*Unified Astronomy Thesaurus concepts:* [Mercury \(planet\) \(1024\)](#); [Space weather \(2037\)](#); [Exosphere \(499\)](#)

## 1. Introduction

Ion bombardment onto the surfaces of airless planetary bodies can sputter atomic and molecular species directly by collisions of nuclei and indirectly through electronic excitations and ionizations. Planetary science studies typically only focus on the direct “knock-on” (also known as collisional, nuclear, or kinetic) component of the sputtering yields (the number of ejected atoms per incident ion). The process of knock-on sputtering has been well characterized using both direct and indirect solutions to the Boltzmann transport equation and by comparisons with experiments (P. Sigmund 1981; H. Hofsäss et al. 2014; P. S. Szabo et al. 2020; H. Biber et al. 2022; C. Bu et al. 2024). However, the process by which ion-induced electronic sputtering is energized is not as well studied.

Ion-induced electronic sputtering broadly refers to the indirect ejection of atoms and molecules by energy transfer events from an incident ion to the electronic structure of a target material. Qualitatively, this process is described as a penetrating ion that deposits electronic energy along its path, leading to a track of excitations and ionizations that store

repulsive energy (i.e., form antibinding states). Neighboring atoms or ions left in repulsive states near the surface can then be ejected directly or, if occurring at depth, can produce a cascade of collisions leading to bond breaking and diffusion (R. E. Johnson 1990). Ion-induced electronic sputtering is one of a few processes that together are commonly categorized as desorption induced by electronic transitions (DIET; V. N. Ageev 1994; Madey et al. 1998). The other two DIET processes are photon-stimulated desorption (PSD) and electron-stimulated desorption (ESD). All three processes produce electronic excitations of surface atoms and ions, leading to the ejections of both neutrals and ions (V. N. Ageev 1994).

In the field of sputtering by particle bombardment, electronic sputtering generally refers to any processes by which particles are ejected due to energy deposited into the electronic structure of a target. Our focus here is on electronic sputtering by keV energy impacts of near-neutral ions. This is to be contrasted with two other cases that we do not consider here. The first is known as potential sputtering and involves highly charged ions at keV energies bombarding insulators. The resulting electronic sputtering yields can be orders of magnitude higher than collisional sputtering (R. Behrisch & W. Eckstein 2007). Considering the composition of the solar wind and the relatively low abundance of highly charged ions therein (R. von Steiger et al. 2000; M. R. Aellig et al. 2001), the resulting sputtering is predicted to be too low to affect the



Original content from this work may be used under the terms of the [Creative Commons Attribution 4.0 licence](#). Any further distribution of this work must maintain attribution to the author(s) and the title of the work, journal citation and DOI.

total sputtering yield (P. Wurz et al. 2022). At higher energies that are relevant for cosmic rays, impacts by MeV or GeV ions of metals result in a significant fraction of the ion energy contributing to localized heating and evaporation through electron–phonon coupling. This too can induce electronic sputtering yields that dominate the purely collisional yields by orders of magnitude (R. Behrisch & W. Eckstein 2007). However, the cosmic-ray flux in the inner solar system is less important compared to the solar wind ion flux (S. P. Sworby 2001).

Here we explore the relative importance of collisional and electronic sputtering, approximated using linear cascade theory (LCT), within the context of solar wind ion irradiation. We focus on the two dominant elements of the solar wind, H and He, at energies typical of the plasma in the near-Mercury space environment. Furthermore, we use Mercury’s Na exosphere as our test case for the relative importance of these two sputtering processes.

Constraining the sputtering of Na atoms from Mercury’s surface is important because observations of temporal and spatial variabilities of the exosphere indicate that solar wind ion precipitation has an effect on the Na distribution. S. Massetti et al. (2017) reported ground-based observations of exospheric Na emission that exhibited variations on a time-scale of minutes near the magnetospheric cusps. Sun et al. (2022) reported MESSENGER observations of an enhancement in Na<sup>+</sup>-group ions during flux transfer event showers near Mercury’s northern magnetospheric cusp, for which they estimated variations in the Na exosphere by more than 10%. Likewise, north–south asymmetries observed in the extended Na tail have been attributed to ion sputtering (A. E. Potter et al. 2002) or PSD enhanced by ion bombardment of the surface (C. A. Schmidt et al. 2012).

Recently, L. S. Morrissey et al. (2022, 2024) used molecular dynamics (MD) to calculate surface binding energies (SBEs) for collisional sputtering and obtained mineral-specific SBE values significantly larger than what has been traditionally used in exospheric simulations. R. M. Killen et al. (2022) showed that exosphere contributions from collisional ion sputtering of an atom with a higher SBE could explain the data of Mercury’s high-altitude Na exosphere above 1000 km. As discussed above, the same incident ions induce both collisional and electronic sputtering. Thus, it is important to understand how efficiently the bombarding ions induce electronic sputtering as compared to collisional sputtering of Mercury’s surface minerals.

Our study revisits previously reported ion-induced sputtering estimates for Mercury obtained from data available in 1986 (M. A. McGrath et al. 1986, hereafter M86) and presents new estimates using more recent data of Mercury’s surface composition and the precipitating ion flux based on observations by the Mercury Surface, Space Environment, Geochemistry and Ranging (MESSENGER; S. C. Solomon et al. 2007) mission. In addition, we use new data more relevant to Mercury’s surface minerals for the nuclear and electronic stopping-power cross sections and the SBEs. LCT is used to estimate collisional and electronic sputtering at Mercury and to motivate the case for further experimental and theoretical studies.

The rest of this article is organized as follows. In Section 2, we review how LCT is applied to estimate both collisional and electronic sputtering yields. Section 3 reviews current knowledge

of the parameters relevant for Mercury that are needed to evaluate the sputtering expressions given in Section 2. Section 4 presents and discusses the results of the sputtering yields evaluated from LCT for the updated parameters. In Section 5, we summarize the implications of the results for interpreting observations of Mercury’s exosphere.

## 2. Sputtering Yield from Linear Cascade Theory

Here, we review the analytical expressions for the collisional and electronic sputtering yields derived from LCT, which uses the binary collision approximation (BCA). Typically, the collisional sputtering yield is estimated using numerical Monte Carlo BCA methods that explicitly track the linear collision cascade as a function of impactor type, energy, and angle. One such model is SDTrimSP, which is based on the transport of ions in matter and can be used in a static or dynamic mode with serial or parallel processing (J. F. Ziegler et al. 2010; A. G. Mutzke et al. 2019).

In this study, LCT is used to estimate both the collisional and electronic sputtering yields. To assess the accuracy of the sputtering yield estimates, we review LCT, emphasizing current knowledge gaps and the need for further studies. LCT has been shown to be applicable to incident ions with energies on the order of  $1 \text{ keV} \lesssim E_A \lesssim 1 \text{ MeV}$  for collisional sputtering, which are presumed to deposit their energy near the substrate surface (P. Sigmund 1981). For electronic sputtering, LCT does not directly account for the energy transfer from the incident ion to the electronic subsystem or the subsequent conversion of electronic energy into translational motion. However, experimental data on electronic sputtering yields indicate that a portion of the electronic energy is converted into translational motion, which initiates a cascade of collisions and sputtering, and that this can be described using LCT when constrained by experimental results (R. E. Johnson & W. L. Brown 1982). These findings suggest that LCT can be used for electronic sputtering initiated by incident ions with energies around  $E_A \lesssim 10 \text{ keV}$ . In the following discussion, variables labeled with subscripts *A* or *B* refer to the ion and target atom quantities, respectively.

Solar wind ions bombard Mercury’s surface with energies of  $\sim 0.05\text{--}13 \text{ keV}$  (J. M. Raines et al. 2022; F. Lavorenti et al. 2023). Most of the precipitating protons impact Mercury’s surface in the cusps and nightside hemisphere with energies of  $\sim 1 \text{ keV}$  (J. M. Raines et al. 2014). For these energies, LCT predicts that the sputtering yield is proportional to the energy deposited by the incident ion. The energy deposited produces a sequence of recoil atoms within the target with kinetic energies  $E_i \ll E_A$ , which does not lead to significant localized heating along the ion track (R. E. Johnson 1990). Depending on the sequence of these collisions, some surface atoms can be imparted energies sufficient to overcome the SBE ( $E_{SB}$ ) and thus be ejected from the target. Analytical expressions of the sputtering yield have been derived from the Boltzmann transport equations. P. Sigmund (1981) gives an overview of the theory of sputtering including solutions to the Boltzmann transport equation and comparisons to experimental data. The application of sputtering theory to planet surfaces and atmospheres is reviewed in R. E. Johnson (1990).

The underlying approximations of the sputtering yield obtained from LCT are (1) collisions in the target are random and result in the slowing down of the incident ions, (2) collisions between atoms in the target material are considered

binary (meaning many body effects are not included), and (3) atomic motions are described with classical mechanics. The general expression of the total sputtering yield for kinetic energy transferred to atoms either directly through knock-on collisions or indirectly through electronic excitations is defined in R. E. Johnson (1990) as

$$Y_i \approx \overline{\Delta z_s}(E_i)/\lambda_i, \quad (1)$$

assuming the energy of recoils exceeds  $E_{SB}$ . The subscript  $i$  is used to refer to either nuclear (n) or electronic (e) sputtering;  $\overline{\Delta z_s}$  is the average sputtering depth and depends on the recoil energy spectrum, the initial depth of the energized atoms, and the SBE; and  $\lambda_i^{-1}$  is the average number of recoils produced per unit path length by the ion (R. E. Johnson 1990). The sputtering depth  $\overline{\Delta z_s}$  is defined for a planar barrier, where the energy of the velocity component directed toward the surface determines ejection, and an isotropic distribution of binary recoils, where their interactions are described by a power-law potential (P. Sigmund 1981; R. E. Johnson 1990). R. E. Johnson (1990) reviews this derivation of  $\overline{\Delta z_s}$  in the appendix to chapter 3, giving

$$\overline{\Delta z_s}(E_i) \approx \frac{3\overline{\lambda_d} E_i}{4\pi^2 E_{SB}}. \quad (2)$$

Here, the average mean free path,  $\overline{\lambda_d}$ , is between collisions of low-energy recoil target atoms (i.e., diffusion) and is given by

$$\overline{\lambda_d} \approx \left( \frac{n_B \sigma_d}{2} \right)^{-1}. \quad (3)$$

This quantity depends on the atomic number density,  $n_B$ , of the target and the momentum transfer collision cross section,  $\sigma_d$  (R. E. Johnson 1990).

Although the yields produced by collisional and electronic sputtering occur simultaneously, theoretically, they are treated separately and additive (R. E. Johnson 1990). In the discussion below, quantities for the collisional yield are defined first, followed by the electronic yield.

### 2.1. Collisional Sputtering Yield

The collisional sputtering yield is defined as  $Y_n$  and given by

$$Y_n \approx \overline{\Delta z_s}(E_n)/\lambda_n, \quad (4)$$

where  $E_n$  is the kinetic energy transferred from an ion to a target particle. The sputtering yield is inversely proportional to the mean distance between energy transfer events,  $\lambda_n$ , which is given by

$$\lambda_n^{-1} \approx E_n^{-1} \left( \frac{dE}{dx} \right)_n = E_n^{-1} S_n n_B. \quad (5)$$

The nuclear stopping cross section,  $S_n$ , can be written in terms of the ion energy loss ( $dE$ ) along its path length ( $dx$ ):

$$S_n \approx n_B^{-1} \left( \frac{dE}{dx} \right)_n. \quad (6)$$

P. Sigmund (1981) showed that the energy dependence of the collisional yield is determined by the nuclear stopping cross section, which describes the incremental energy transfer events  $dE$  along an ion's path  $dx$  by elastic collisions with target atoms. The stopping cross section as given in

Equation (6) is a proportionality constant that relates the energy loss per unit path length to the target density. Combining everything together, we find that the nuclear sputtering yield is independent of the number density of the target (P. Sigmund 1981; R. E. Johnson 1990):

$$Y_{n,M} \approx \frac{3\alpha S_n}{2\pi^2 \sigma_d E_{SB}} = (4.2 \times 10^{14} \text{ cm}^{-2}) \frac{\alpha S_n}{E_{SB}}. \quad (7)$$

P. Sigmund (1981) writes this sputtering yield expression including a factor  $\alpha$ , which is a correction factor for momentum exchange between the incident ion and target atoms, and the nuclear sputter yield as written in M86 is given on the right-hand side of Equation (7). The  $\alpha$  factor can be constrained empirically from experiments and has been shown to depend on the ion incidence angle, the ion energy, and the mass ratio of the target atom and incident ion (P. Sigmund 1981; R. E. Johnson 1990). The momentum transfer cross section,  $\sigma_d$ , for the low-energy recoils is chosen to be  $\sigma_d = 3.6 \times 10^{-16} \text{ cm}^2$ , obtained from a power-law approximation to the Thomas–Fermi model cross section and sputtering experiments for metals (P. Sigmund 1969; their Equation (96)); which we expect to be within a factor of 3 for minerals. Lastly, the expression of the yield defined here assumes a target surface with planar binding and is roughly consistent with experiments for sputtering of polycrystalline metals by keV ions (P. Sigmund 1981).

### 2.2. Electronic Sputtering Yields

Electronic sputtering can be induced by ionizations and electronic excitations produced in a substrate at depth by ion impacts. If a repulsive state is produced near, but below, the surface, the energized atoms can initiate a mini cascade of collisions. In this event, previous studies have shown that the general expression for the yield can be approximated using the same form as the LCT collisional sputtering yield (R. E. Johnson & W. L. Brown 1982; W. L. Brown & R. E. Johnson 1986; R. E. Johnson 1990),

$$Y_e \approx \overline{\Delta z_s}(E_e)/\lambda_e, \quad (8)$$

where  $E_e$  is the average repulsive energy transferred to the kinetic energy of a target atom and  $E_e \ll E_A$ . Here, the mean free path between energizing events,  $\lambda_e$ , is the average distance between ionizations induced along the ion track:

$$\lambda_e^{-1} = n_B \sigma_i = n_B \frac{(dE/dx)_e}{n_B W} = n_B \frac{S_e}{W}. \quad (9)$$

This distance depends on the ionization cross section,  $\sigma_i$ , which we approximate by the ratio of the electronic stopping cross section,

$$S_e \approx n_B^{-1} \left( \frac{dE}{dx} \right)_e, \quad (10)$$

to the average energy  $W$  expended by the ion that produces the ionization (W. L. Brown et al. 1984). The electronic stopping cross section describes energy loss by the incident ion due to inelastic collisions, such as slowing because of electron interactions.

As some of the electronic energy is expended in vibrations and phonon excitations, the quantity  $W$  is fractionally higher than the ionization energy required to produce an electron–hole pair (R. E. Johnson 1990). We note that R. E. Johnson (1990)

showed that fast electrons and ions induce more ionizations than excitations in many materials. Taking the ratio of the sputtering depth and mean free path for electronic excitations gives the electronic sputtering yield

$$Y_e \approx \frac{3}{2\pi^2\sigma_d} \frac{S_e}{W} \frac{E_e}{E_{SB}} = (4.2 \times 10^{14} \text{cm}^{-2}) \frac{S_e}{W} \frac{E_e}{E_{SB}}. \quad (11)$$

Here the  $\alpha$  factor is not included in Equation (11) because electronic sputtering is not directly driven by momentum transfer between the incident ion and target atoms.

This derivation starting from Equation (8) can be compared to the results of M86 by defining the sputter depth as

$$\overline{\Delta z_s}(E_e) = P_e n_B^{-1/3}, \quad (12)$$

where

$$P_e = \frac{3}{2\pi^2} \frac{E_e}{E_{SB}}, \quad (13)$$

and the collision cross section is approximated as  $\sigma_d \sim n_B^{-2/3}$  (P. Sigmund 1969; M86; R. E. Johnson 1990). The variable  $P_e$  is referred to as a sputtering factor, and its derivation is reviewed in chapter 3 of R. E. Johnson (1990). Making the appropriate substitutions into Equation (8), the electronic sputtering yield as defined in M86 can then be written as

$$Y_{e,M} \approx P_e n_B^{\frac{2}{3}} \sigma_i, \quad (14)$$

which is equivalent to that in Equation (11).

### 2.3. Sputtering Yields for Inhomogeneous Targets

The yields given by Equations (7) and (14) are defined for monoatomic targets, but the expressions are roughly applied to inhomogeneous targets by multiplying the yield by the surface fraction  $f_X$  of the species  $X$  of interest so that

$$Y_{n,X} = f_X \cdot Y_{n,M} \quad (15)$$

and

$$Y_{e,X} = f_X \cdot Y_{e,M}. \quad (16)$$

Equations (15) and (16) are used to calculate the collisional and electronic sputtering yields, respectively, in Section 4 for the Mercury-relevant parameters discussed in Section 3.

## 3. Mercury Sputtering Parameters

In this section, we review the differences of the sputtering yield parameters used in our study and those used in M86 (see Table 1). The parameters discussed in this section will be used in Equations (15) and (16) to calculate the sputtering yields presented in Section 4. Since the study of M86, there have been new observational updates on Mercury's environment, and there have been improvements in the methods used to estimate stopping-power cross sections for ion interactions with substrates. First, we comment on the parameters that we directly adopted from M86 and are not well constrained for Mercury-relevant minerals; then we review the updated parameters.

To estimate the collisional sputtering yield of Na from Mercury surface minerals, the values for  $\alpha$  and  $E_{SB}$  were taken from M86. As discussed in Section 2.1, the parameter  $\alpha$  can be obtained from fits to experimental yields, which indicate that  $\alpha$  has an empirical dependence on the ratio of the target mass to

**Table 1**  
Collisional and Electronic Sputtering Parameters

Parameter	This Study	M86
$\alpha$		1
$W$ (eV)		20–30
$P_e$		0.1
$E_{SB}$ (eV)	See Figure 3	2
$S_n$ (eV cm <sup>2</sup> )	See Figure 1	(H) $5 \times 10^{-16}$ (He) $3 \times 10^{-15}$
$S_e$ (eV cm <sup>2</sup> )	See Figure 1	(H) $3 \times 10^{-15}$ (He) $2 \times 10^{-15}$ <sup>a</sup>
$n_B^{2/3}$ (atoms cm <sup>2</sup> )	$7.4 \times 10^{14}$	$2.5 \times 10^{15}$
$f_{Na}$	0.02–0.05	0.002

<sup>a</sup> This value of  $S_e$  for He is a factor of 10 smaller than the value reported in M86 ( $2 \times 10^{-14}$  eV cm<sup>2</sup>). We believe the latter is a typo in M86 because using the smaller  $S_e$  to evaluate the electronic sputtering yield is required to obtain the electronic sputtering yield,  $Y_{e,Na} = 4 \times 10^{-5}$ , for He reported in the M86 manuscript.

the incident mass. However, there are no experimental data available for this parameter for Mercury-relevant surface minerals. P. Sigmund (1981) derived an analytical expression for  $\alpha$  and showed that the term is on the order of 1 for protons incident on heavy targets. Likewise, R. E. Johnson (1990) showed experimental data that indicate that  $\alpha$  increases with increasing mass ratio up to  $M_B/M_A = 20$ , for which the data indicate  $\alpha \approx 0.75$ . Both studies emphasize that these values should be considered rough estimates. We took  $\alpha = 1$ , as Na sputtered from feldspar by H<sup>+</sup> has a mass ratio of  $M_B/M_A = 23$ . Second, based on the composition of lunar rocks, M86 assumed that Na is bound to O in the form of NaAlSi<sub>3</sub>O<sub>8</sub> (the albite end-member of plagioclase feldspar) with an estimated SBE of 2 eV. The SBE is an important parameter that is not well constrained. This parameter affects both the magnitude of the sputtering yield and the energy distribution of sputtered atoms. Therefore, we first adopted the same value used in M86 for comparison; subsequently, we considered the SBEs of Na bound in various silicate minerals, as derived from recent MD simulations by L. S. Morrissey et al. (2024).

To estimate the electronic sputtering yield, first we directly take  $P_e$  and  $W$  from M86, as the values are not known for Mercury-relevant surface minerals. The efficiency factor is taken to be  $P_e \lesssim 0.1$ , which is based on fits of experimental data of H<sub>2</sub>O yields from water-ice films (R. E. Johnson et al. 1984). This factor is used to account for the fraction of the deposited electronic energy that goes into the nuclear motion of target atoms. Second, R. E. Johnson (1990) reports values for  $W$  that range from 20–44 eV, as obtained for atomic and molecular gases. These values are unknown for atomic and molecular species in Mercury-relevant surface minerals; so to compare to M86, we use the same values that they used.

Since the M86 study, there have been advances in the estimates of nuclear and electronic stopping-power cross sections, which define how much energy is lost or transferred by an ion to a target atom along the path of the ion. These quantities depend on the incident ion mass and energy and the target composition. SRIM had a major update to its calculations of stopping-power cross sections in 1998 that included comparisons to experimental data for over 100 compounds. In addition, SRIM uses Bragg's rule to calculate the stopping-power cross sections of protons and other ions

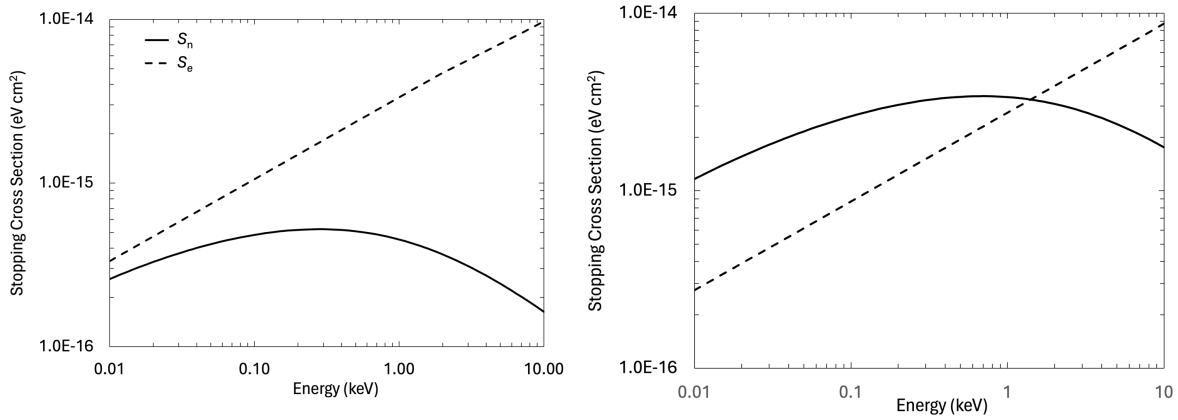


**Figure 1.** The nuclear (solid line) and electronic (dashed line) stopping-power cross sections for H (left) and He (right) obtained for albite using SRIM 2008.

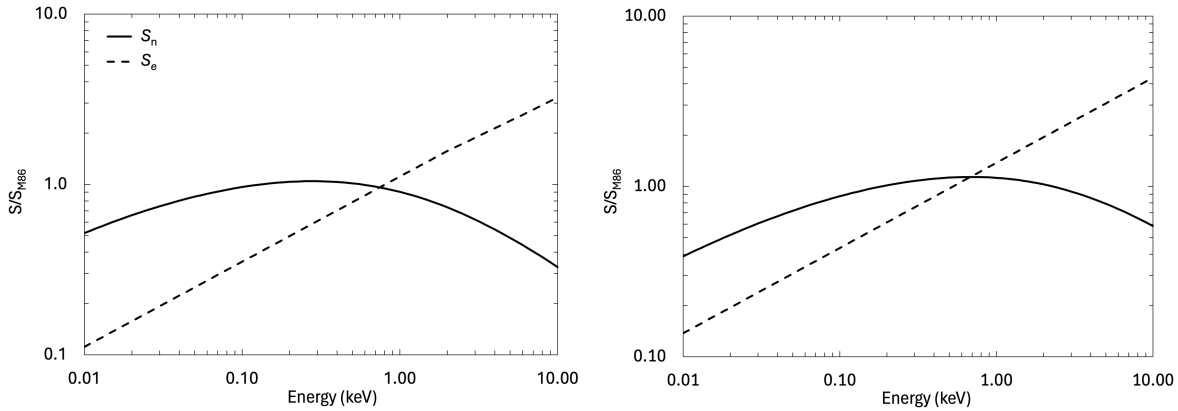


**Figure 2.** Ratio of the SRIM 2008 to M86 values for the nuclear (solid line) and electronic (dashed curve) stopping energy cross sections in albite for H (left) and He (right).

incident on compounds for which experimental constraints are not available (J. F. Ziegler et al. 2010). Where experimental data are lacking, the stopping-power cross section for the compound is approximated using the cross sections of the individual elements, which does not account for changes in atomic bonding due to the compound. We are unaware of any published experimental stopping-power cross-section data for albite, so we used SRIM 2008 (J. F. Ziegler et al. 2010) to approximate the values for  $S_n$  and  $S_e$  of incident H and He ions, shown in Figure 1. This is to be contrasted with the M86 study, which did not specify the ion energies or target material for their stopping-power cross sections.

Here, we consider incident H and He ion energies ranging from 0.05 to 13 keV for calculating  $S_n$  and  $S_e$ . These constraints are based on measurements from MESSENGER’s Fast Imagine Plasma Spectrometer (FIPS) for the  $H^+$  and  $He^{++}$  flux over Mercury’s northern magnetospheric cusp (J. M. Raines et al. 2022; J.-T. Zhao et al. 2024) and theoretical models for solar wind ion precipitation onto the planet (F. Lavorenti et al. 2023). The FIPS data indicated that the flux was highly variable, with most ions at energies near 1 keV  $amu^{-1}$ . At this energy, the penetrating ions lose much of their energy due to electronic stopping within surface grains (see Figure 1). For H, the electronic stopping cross section dominates the nuclear stopping cross section over the entire energy range and is almost an order of magnitude larger at 1 keV. For He, nuclear stopping is dominant up to energies of  $\sim 1$  keV. At the mean energy of He ions in the unperturbed solar wind of 4 keV,  $S_e$  is over 50% larger than  $S_n$ .

The ratios of the stopping-power cross sections used in this study relative to M86 are shown in Figure 2. The main difference between the two is for the electronic stopping cross sections. This difference can be more than an order of magnitude for both H and He in the energy range considered. However, at the nominal solar wind energy of 1 keV  $amu^{-1}$ , the electronic stopping cross sections used in both studies are comparable for H but differ by a factor of 3 for He.

Since the work of M86, MESSENGER observations have enabled us to derive updated values for the surface atomic density  $n_B^{2/3}$  and surface Na fraction  $f_{Na}$ . The estimates of M86 were based on lunar data. Since that study, R. M. Killen et al. (2022) estimated  $n_B^{2/3} \approx 7.4 \times 10^{14}$  atoms  $cm^{-2}$  based on a mass density estimated from lunar grains but using an average atomic mass determined from the stoichiometry inferred from MESSENGER observations of the surface composition (L. R. Nittler et al. 2011). This value of  $n_B^{2/3}$  is approximately a factor of 3 lower than that of the M86 study. Furthermore, MESSENGER observations of the surface composition at the equator and northern latitudes indicate a surface Na fraction of  $f_{Na} = 0.02\text{--}0.05$  (P. N. Peplowski et al. 2015; L. R. Nittler & S. Z. Weider 2019). This is more than an order of magnitude larger than what was used in M86.

## 4. Results and Discussion

### 4.1. Sputtering Yields

In this section, we discuss the Na sputtering yield obtained using Equations (15) (nuclear) and (16) (electronic) with the

**Table 2**  
Sputtering Yields

Yield (Na Atoms/Ion)	$f_{\text{Na}}$	Nuclear		Electronic	
		H	He	H	He
This study <sup>a</sup>	0.02–0.05	$2\text{--}5 \times 10^{-3}$	$1\text{--}3 \times 10^{-2}$	$2\text{--}6 \times 10^{-4}$	$4\text{--}10 \times 10^{-4}$
M86	0.002	$2 \times 10^{-4}$	$1 \times 10^{-3}$	$6 \times 10^{-5}$	$4 \times 10^{-5}$

<sup>a</sup> The yields are evaluated for ion energies of 1 keV amu<sup>-1</sup>.

parameters given in Table 1. As mentioned in Section 2, SDTrimSP and similar BCA Monte Carlo models are more accurate than LCT for collisional sputtering yields. However, the authors are unaware of any similar approach to estimate the electronic sputtering yield. Hence, for consistency, in the following discussions, we compare the nuclear and electronic sputtering yields evaluated with LCT.

The Na sputtering yields obtained for an incident ion energy of 1 keV amu<sup>-1</sup> using our updated parameters and those obtained using the M86 parameters are compared in Table 2 and Figure 3. We obtained nuclear and electronic sputtering yields for H and He approximately an order of magnitude larger than the values obtained using the M86 parameters. Concerning the nuclear sputtering yields, our values for  $S_n$  for H and He with energy 1 keV amu<sup>-1</sup> are similar to the values given in M86, and for this comparison, we used an SBE of 2 eV as given in M86. Therefore, the difference in our result for nuclear sputtering yields compared in Table 2 is due primarily to the larger Na fraction based on MESSENGER data. Below, we discuss results for the nuclear sputtering yields evaluated using SBE values derived for recent MD studies (L. S. Morrissey et al. 2024).

Concerning the electronic sputtering yield, it depends on the Na fraction, electronic stopping cross section, and surface atomic density. We obtained electronic sputtering yields for H that are a factor of 3–10 larger than those obtained using the M86 parameters due to the product of the larger Na fraction and smaller surface atomic density based on MESSENGER data. The electronic sputtering yields for He are also approximately an order of magnitude larger than the M86 yields because our updated value for  $S_e$  is a factor of 3 larger, which cancels out the difference due to our lower value for  $n_B^{2/3}$ .

One major source of uncertainty in estimating the nuclear sputtering yield is the SBEs for Na atoms in silicate minerals relevant to Mercury. The nuclear sputtering yields in Table 2 were calculated using an SBE of 2 eV, as suggested for albite in M86. This is to be contrasted with the L. S. Morrissey et al. (2022) MD study, which derived an SBE of 7.9 eV for the perfect cleavage (001) plane of albite, denoted using the Miller indices. The MD results with SBEs closest to 2 eV, suggested in M86, were for pure Na (1.4 eV) and Na<sub>4</sub>SiO<sub>4</sub> (2.6 eV), both of which are not expected to be found on the surface of Mercury. In a more recent MD study, L. S. Morrissey et al. (2024) showed that the SBE of surface atoms varies significantly with crystallographic surface orientation and that the SBE of Na atoms in albite varies from 4.1 to 10.7 eV.

In Figures 3(a) and (b), we show nuclear Na yields obtained using the SBEs for Na atoms in different surface orientations for albite from L. S. Morrissey et al. (2024) and compared to

the M86 value. As discussed above, MESSENGER observations indicate a global surface,  $f_{\text{Na}} = 0.02\text{--}0.05$ , with a significant fraction of Na inferred to be bound in plagioclase feldspar minerals such as labradorite, which is an intermediate solid solution between albite and anorthite (the Ca end-member of plagioclase feldspar). To compare the nuclear sputtering yields calculated using Equation (15) with the SDTrimSP results for albite in L. S. Morrissey et al. (2024), we scaled the nuclear sputtering yields by  $f_{\text{Na}}/(1/13)$ . The fraction of Na in the albite compound is  $(1/13)$ , and the error bars in Figures 3(a) and (b) represent the upper and lower limits of the SDTrimSP nuclear yields scaled to the MESSENGER-derived surface fraction,  $f_{\text{Na}} = 0.02\text{--}0.05$ . There is good relative agreement between the LCT nuclear sputtering yields calculated using Equation (15) and the SDTrimSP results in L. S. Morrissey et al. (2024) for surface orientations (001) (blue error bar), (010) (red error bars), and (110) (gray error bars). The multiple SDTrimSP results shown for a particular cleavage plane indicate the different surface positions that can be occupied by a Na atom, each with a distinct SBE resulting from its local chemical bonding (L. S. Morrissey et al. 2024). We take this as an estimate for the accuracy of the LCT model. For our comparisons to the M86 nuclear sputtering yields for H and He in Figures 3(a) and (b) (represented with the symbol  $\times$ ), we used the MESSENGER-derived values for  $f_{\text{Na}}$  and  $S_n$  for albite obtained from SRIM 2008, which results in our much larger nuclear sputtering yields calculated using Equation (15).

Despite the relative agreement shown here, in general, using SDTrimSP or similar Monte Carlo models that apply BCA is favored over the analytical expression for the nuclear sputtering yield from LCT. The major reason is the use of more complex potentials in BCA models, such as the Ziegler–Biersack–Littmark potential, compared to the Thomas–Fermi potential to describe atomic interactions in the analytical expression (P. Sigmund 2017). Furthermore, BCA models explicitly track atomic trajectories and scattering and more accurately account for the target density of specific materials.

Over the range of ion energies measured by FIPS,  $\sim 0.05\text{--}13$  keV, the nuclear sputtering yields are significantly larger than the electronic sputtering yields for almost all energies considered (see Figure 4). This comparison is independent of the SBE as both the nuclear and electronic sputtering yields have the same dependence with  $E_{\text{SB}}$ . Furthermore, due to its larger nuclear stopping cross section, the yield for He is approximately an order of magnitude larger than that for H. The electronic sputtering yields are similar for H and He. However, considering the H/He abundance ratio in the solar wind is typically larger than  $\sim 20$ , both the nuclear and electronic Na sputtering fluxes are larger for protons impacting the surface than for He ions. The FIPS energy spectra that indicate precipitating protons have mean energies of  $\sim 1$  keV (J. M. Raines et al. 2014). However, our results further highlight that detailed information on the composition and energy spectra of the precipitating ion flux is needed for comprehensive studies of the contribution of sputtering to Mercury’s exosphere.

#### 4.2. Ejecta Energy Distribution

In addition to the yields, the ejecta energy spectra from nuclear and electronic sputtering are important to consider when evaluating the contribution of the Na sputtering rates to

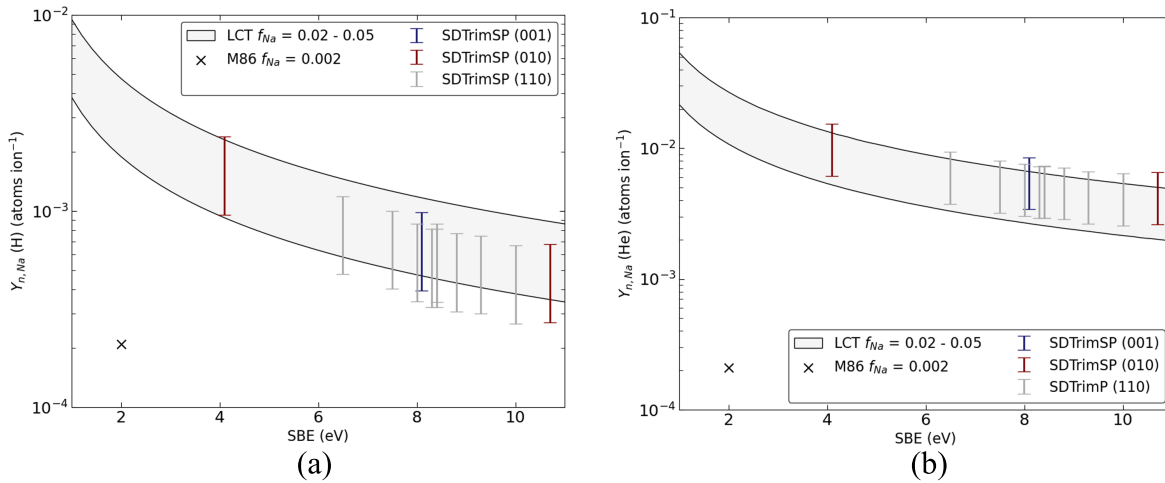


**Figure 3.** Comparison of the nuclear Na yield plotted as a function of Na SBE for (a) 1 keV H ions and (b) 4 keV He ions impacting albite, as obtained from LCT here and in M86 and from SDTrimSP BCA simulations (L. S. Morrissey et al. 2024). The gray-shaded regions for the LCT results and the error bars for the SDTrimSP results indicate the range of sputtering yields for the MESSENGER-derived Na surface fraction of  $f_{Na} = 0.02\text{--}0.05$ . See text for details.

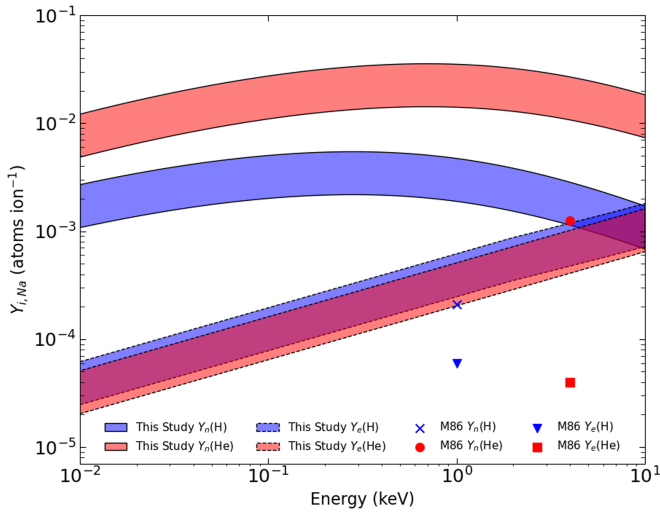


**Figure 4.** The Na sputtering yield evaluated using LCT as a function of incident ion energy for H and He ions evaluated using Equations (15) and (16) and compared to M86. Equations (15) and (16) were evaluated using the parameters in Table 1. For our comparison to M86, we also used  $SBE = 2$  eV.

Mercury’s exosphere. The energy spectra from nuclear sputtering, which peaks at half the SBE, are well described by the Sigmund–Thompson distribution. Based on the MD-derived SBEs for Na bound in different silicates from L. S. Morrissey et al. (2022, 2024), a significant population of atoms ejected by nuclear sputtering are capable of escaping Mercury’s gravity (the escape energy is  $\sim 2.1$  eV). In a recent study by R. M. Killen et al. (2022), they found that the Na column densities observed by MESSENGER are consistent with nuclear sputtering from a high-SBE surface material such as feldspar with values on the order of  $SBE = 7.9$  eV. Their exosphere model results indicate that Na ejected from nuclear sputtering could contribute to the high-altitude ( $\gtrsim 1000$  km) exosphere in amounts comparable to micrometeoroid impact vaporization (IV). This is the case even though the ejecta energy distribution for IV, which is described by a Maxwell–Boltzmann energy distribution, has a much lower characteristic energy of 0.3 eV (C. A. Schmidt et al. 2012; R. M. Killen et al. 2022).

The relative contribution of the electronic sputtering flux to Mercury’s exosphere should be compared with that of the

other DIET processes. M. Sarantos et al. (2010) estimated PSD energy spectra by fitting lunar exosphere Na density profiles obtained from ground-based observations of D1 and D2 emission lines, finding that the source matches a Maxwell–Boltzmann distribution with a temperature of 1200 K (with a peak energy of  $\sim 0.1$  eV). This value is similar to the ejecta energy peaks for potassium (with peak energies 0.12–0.39 eV) from PSD studies of K adsorbed on  $Cr_2O_3$  (T. E. Madey et al. 1998), although the spectra were found not to be Maxwellian. In the K PSD experiments, the lowest value was measured for a fully saturated surface, while the highest corresponds to fractional coverage. The PSD measurements are also comparable to data from ESD experiments of Na adsorbed on  $SiO_2$  and lunar basalts that measured similar peak values of 0.12 eV and 0.08 eV, respectively (B. V. Yakshinskiy & T. E. Madey 2000, 2005). We are unaware of any subsequently published measurements of PSD ejecta energy spectra for Na adsorbed on oxides or silicates.

It has been suggested that all DIET processes should be similar because all the processes involve electronic excitations that drive the repulsive energy leading to the ejection of atoms (V. N. Ageev 1994; B. V. Yakshinskiy & T. E. Madey 2005). Therefore, Na atoms ejected by electronic sputtering are likely to have energy spectra more comparable to PSD and ESD as opposed to nuclear sputtering. The energy spectra of Na ejected by PSD is likely an upper limit of the DIET processes because electrons and ions penetrate to larger depths and there is more energy dissipation to the bulk (V. N. Ageev 1994). We are not aware of any experiments that measured the ion-induced electronic sputtering of Na for Mercury-relevant minerals. It is widely accepted that PSD is the dominant source of Na atoms to the dayside exosphere at low altitudes. However, the contribution of electronic sputtering to nightside exosphere densities and the inventory of surface Na atoms, where PSD is not active, is not well characterized.

#### 4.3. Comparison to Other Exosphere Sources

Based on our results for the sputtering yields in Table 2 and Figure 3 and their respective energy spectra, we qualitatively consider the sputtering rates to Mercury’s exosphere. In the J. M. Raines et al. (2022) analysis of FIPS measurements, they found that protons access the surface in the northern cusp at a

mean latitude of  $63^{\circ}$ – $68^{\circ}$  with an average flux of  $\sim 10^7$   $\text{cm}^{-2} \text{s}^{-1}$ . However, because of the MESSENGER orbit, FIPS could not sample the proton flux in the southern cusp. S. Fatemi et al. (2020) reproduced both the northern cusp area and precipitating proton fluxes comparable to that inferred from MESSENGER measurements using a hybrid model. In their study, they also tracked protons that accessed both the northern and southern cusps as well as the nightside hemisphere. They calculated a total proton incidence rate in the range of  $10^{25}$ – $10^{26}$   $\text{ions s}^{-1}$  depending on the orientation of the interplanetary magnetic field. Similar results were obtained in a separate hybrid model study by J. Guo et al. (2023) that focused on the properties of the disappearing dayside magnetosphere. Here we estimate the total sputtering rates of Na atoms using the proton precipitation rates given in S. Fatemi et al. (2020). We use the nuclear sputtering yields evaluated using Equation (15) for an incident ion energy  $E_i = 1$  keV and SBE values of 3 eV and 7.9 eV. The choice of  $E_i$  is based on the FIPS energy spectra that indicate that precipitating protons have mean energies of 1 keV (J. M. Raines et al. 2014). The choice of the SBE value is more challenging, because Mercury’s surface minerals have varying degrees of crystallinity due to space weathering, impact gardening, and ballistic Na atoms that are readsorbed on the surface, so the Na surface atoms possess a distribution of SBEs. Therefore, we consider SBE values corresponding to adsorbed (SBE = 3 eV) and bound (SBE = 7.9 eV) Na (L. S. Morrissey et al. 2025). L. S. Morrissey et al. (2025) used MD to calculate the SBEs for Na atoms adsorbed onto the surface of  $\text{SiO}_2$  and obtained values as low as 1–3 eV, depending on surface coverage. A significant fraction of Na atoms ejected by PSD, IV, and electronic sputtering have ballistic trajectories that return and adsorb on the surface. This is to be contrasted with SBEs as high as 7.9 eV for Na atoms bound in albite obtained using a similar MD approach in L. S. Morrissey et al. (2024). Using this range of SBEs, corresponding to nuclear sputtering yields of  $1.2$ – $3.2 \times 10^{-3}$  atoms  $\text{ion}^{-1}$  (Table 2 and Figure 3), we obtain a nuclear sputtering rate of  $1.3$ – $2.6 \times 10^{23}$  atoms  $\text{s}^{-1}$ . As discussed in R. M. Killen et al. (2022), this nuclear sputtering source should be distinguishable from the total IV source rate of  $10^{22}$ – $10^{23}$  atoms  $\text{s}^{-1}$  at high altitudes in the exosphere.

To consider the source of atoms ejected from electronic sputtering, using an electronic sputtering yield of  $6 \times 10^{-4}$  atoms  $\text{ion}^{-1}$  (Table 2 and Figure 3), we obtain a total electronic sputtering rate of  $6 \times 10^{22}$  atoms  $\text{s}^{-1}$ . This result is obtained using the total proton flux into the cusps and nightside hemisphere calculated by the S. Fatemi et al. (2020) hybrid model. Globally, this is to be compared to PSD, which is active on the dayside hemisphere, ejects a total of  $10^{24}$ – $10^{25}$  atoms  $\text{s}^{-1}$  (C. A. Schmidt et al. 2012; R. M. Killen et al. 2022), and is approximately 2–3 orders of magnitude larger than electronic sputtering. However, on Mercury’s nightside, where PSD does not operate, the S. Fatemi et al. (2020) results indicate that magnetotail reconnection can supply up to 60% of the total precipitating proton rate to the surface, corresponding to an electronic sputtering rate of up to  $3.6 \times 10^{22}$  atoms  $\text{s}^{-1}$ . Global transport models that track the sources of Na atoms released in the exosphere and deposited on the surface should investigate the potential to distinguish the nightside exosphere and surface inventory due to electronic sputtering.

#### 4.4. Limitations in Mercury Sputtering Calculations

Several of the approximations used to make the sputtering yield calculations feasible should be considered carefully when applying the values to exospheric models to compare with observations. Below, we list the uncertainties in our calculations.

1. *Stopping-power cross sections.* The values for  $S_n$  and  $S_e$  used from SRIM 2008 were estimated for the albite compound by using Bragg’s rule. This approximation ignores the effect of chemical bonds on the stopping power, which may significantly impact the values of  $S_n$  and  $S_e$ .
2. *SBE.* The SBE depends on the properties of the mineral lattice and its composition and absorbate coverage (L. S. Morrissey et al. 2025). The nuclear sputtering yield calculated via LCT was found to vary by over an order of magnitude across the range of SBEs depicted in Figure 3. These calculations were based on SBEs derived from MD simulations of Na chemically bound in albite. However, Mercury’s surface likely possesses a broad distribution of SBEs. Future investigations should examine the uncertainties inherent in using a single characteristic SBE versus a full energy distribution when modeling the exospheric sputter contribution for comparison to observations.
3. *Surface density and Na fraction.* While the values for  $n_B^{2/3}$  and  $f_{\text{Na}}$  have been updated since the M86 study based on MESSENGER data, the mass density used to estimate the total surficial density is still approximated using lunar values. Furthermore, the range of values for  $f_{\text{Na}}$  was solely based on observations at the equator and northern latitudes. Broader observations, potentially during the BepiColumbo mission, are required to obtain more representative values to further constrain the sputter yields.
4. *Electronic sputtering efficiency.* The efficiency factor for electronic sputtering,  $P_e$ , has not been characterized for either lunar samples or Mercury-analog samples. Here, the value used was derived from experiments involving the electronic sputtering of thin film ices (R. E. Johnson et al. 1984; W. L. Brown & R. E. Johnson 1986; R. E. Johnson 1990). The proportion of electronic energy that leads to minicollision cascades and ultimately sputtering cannot be directly determined by LCT or BCA models. Instead, it must be characterized experimentally or via advanced simulations that account for energy deposition into substrate electrons, such as time-dependent density functional theory (M. E. Casida & M. Huix-Rotllant 2012) or nonadiabatic MD (F. Agostini & B. F. E. Curchod 2019). The challenge for any new experiments is to accurately measure the energy distribution of ejected atoms, enabling the distinction between electronic and nuclear sputtering. Typically, electronic sputtering results in ejected atoms with energies around 0.1 eV, while nuclear sputtering produces energies in the 2–10 eV range; see Figure 3. Computationally, modeling these processes is further complicated by the different relaxation timescales of the electronic system compared to the translational motion of atoms.

Both the nuclear and electronic sputtering yields calculated using LCT vary linearly with the parameters discussed above. Therefore, future experimental and theoretical studies are needed to refine the parameters to disentangle the potential sputtering contributions in observations of Mercury's exosphere. See Section 2 for details on the calculation of the nuclear and electronic sputtering yields using the parameters discussed above.

## 5. Conclusion

In this study, we have revisited the sputtering yields given in M86 from LCT with updated values for Mercury's surface density and Na surface fraction based on MESSENGER data and recent stopping-power cross sections obtained from SRIM 2008. The major differences between yield estimates are the factor of 10 larger Na surface fraction, the factor of 3 lower total atomic surface density, and the factor of 3 larger  $S_e$  for He used in our study based on MESSENGER data and stopping-power cross-section data that were not available during the M86 study. When consistent parameters for  $S_n$  and SBE are used, the nuclear sputtering yields calculated with LCT show strong agreement with the results obtained from SDTrimSP.

There are ongoing investigations into the parameters to use to estimate the nuclear sputtering yields. These works include MD studies of the SBEs for relevant silicate minerals (L. S. Morrissey et al. 2022, 2024, 2025), experiments to constrain the ejecta angular distribution (C. Bu et al. 2024), new SDTrimSP calculations to estimate the nuclear sputtering yield using the MD SBEs (L. S. Morrissey et al. 2023, 2024), and exosphere models that implement all these parameters to track the distribution of Na in Mercury's exosphere to compare with observations (R. M. Killen et al. 2022). As discussed in R. M. Killen et al. (2022), in situ observations of Na at high altitudes (>1000 km) could distinguish the contributions of nuclear sputtering and IV. New experiments of the Na sputter yield and ejecta distribution for Mercury-relevant minerals as a function of crystallinity, to constrain MD studies, are needed to investigate the distribution of SBEs for Na expected for quasicrystalline surface minerals. There is agreement in the Na SBE between the MD-derived values and those from secondary ion sputtering experiments of Na ions sputtered from nepheline ( $\text{NaAlSi}_3\text{O}_8$ ) by R. Martinez et al. (2017). However, the MD SBEs are derived for neutrals, whereas the Martinez et al. experiments obtained energy spectra for secondary ions (L. S. Morrissey et al. 2022). Furthermore, R. C. Wiens et al. (1997) conducted experiments that measured the velocity distribution of sputtered neutrals from sodium sulfate,  $\text{Na}_2\text{SO}_4$ , for which Na is primarily bound to O, similar to silicates. However, they derived a peak energy of 0.27 eV (SBE = 0.54 eV), which is inconsistent with the SBE for nuclear sputtering obtained in the MD studies.



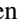


The current state of understanding of electronic sputtering is insufficient to constrain its contribution to Mercury's exosphere. Considering ion-induced electronic and nuclear sputtering concomitantly with very different characteristic energies, new experimental setups capable of accurately measuring the energy spectra of sputtered neutrals and/or ions over a broad energy range are needed. Electronic sputtering is expected to peak at energies on the order of 0.1 eV and nuclear sputtering at energies on the order of several eV. Disentangling how the two contributions to the

energy spectra overlap is important to extract information on electronic sputtering. In addition, new exosphere simulations of electronic sputtering that track the temporal evolution of the inventory of Na cycling between the exosphere and surface, especially on the nightside, could provide additional insight into this process.

## Acknowledgments

O.J.T., M.J.B., R.M.K., and D.W.S. were supported in part by NASA Solar System Workings Program Award grant No. 80NSCC22K0099. O.J.T. was also supported in part by the Goddard Space Flight Center, Internal Science Funding Model project, Exosphere Ionosphere Magnetosphere Modeling. L.S.M. was supported in part by the NSERC Discovery grant and the CSA Research Opportunities in Space Sciences award No. 23EXPROSS3. Robert E. Johnson is acknowledged for providing useful comments on the manuscript. United States Naval Academy Summer intern Cole Martin is acknowledged for helping with the sputtering yield calculations used in the manuscript.

## ORCID iDs

Orenthal J. Tucker  <https://orcid.org/0000-0002-8235-5440>  
 Liam S. Morrissey  <https://orcid.org/0000-0001-7860-9957>  
 Rosemary M. Killen  <https://orcid.org/0000-0002-0543-2326>  
 Matthew H. Burger  <https://orcid.org/0000-0002-9334-7198>  
 Ronald J. Vervack Jr.  <https://orcid.org/0000-0002-8227-9564>  
 Daniel W. Savin  <https://orcid.org/0000-0002-1111-6610>

## References

- Aellig, M. R., Lazarus, A. J., & Steinberg, J. T. 2001, The Solar Wind Helium Abundance: Variation with Wind Speed and the Solar Cycle, *GeoRL*, **28**, 2767
- Ageev, V. N. 1994, Desorption Induced by Electronic Transitions, *PrSS*, **47**, 55
- Agostini, F., & Curchod, B. F. E. 2019, Different flavors of nonadiabatic molecular dynamics, *WIREs Comput. Mol. Sci.*, **9**, 1
- Behrisch, R., & Eckstein, W. 2007, in *Sputtering by Particle Bombardment*, ed. Ascheron, Vol. 110 (Berlin: Springer-Verlag)
- Biber, H., Brötzner, J., Jäggi, N., et al. 2022, Sputtering Behavior of Rough, Polycrystalline Mercury Analogs, *PSJ*, **3**, 271
- Brown, W. L., Augustyniak, W. M., Marcantonio, K. J., et al. 1984, Electronic Sputtering of Low Temperature Molecular Solids, *NIMPB*, **1**, 307
- Brown, W. L., & Johnson, R. E. 1986, Sputtering of Ices: A Review, *NIMPB*, **13**, 295
- Bu, C., Morrissey, L. S., Bostick, B. C., et al. 2024, Absolute Doubly Differential Angular Sputtering Yields for 20 KeV Kr+ on Polycrystalline Cu, *JAP*, **135**, 035302
- Casida, M. E., & Huix-Rotllant, M. 2012, Progress in Time-Dependent Density-Functional Theory, *ARPC*, **63**, 287
- Fatemi, S., Poppe, A. R., & Barabash, S. 2020, Hybrid Simulations of Solar Wind Proton Precipitation to the Surface of Mercury, *JGRA*, **125**, 1
- Guo, J., Lu, S., Lu, Q., et al. 2023, Three-Dimensional Global Hybrid Simulations of Mercury's Disappearing Dayside Magnetosphere., *JGRE*, **128**, 1
- Hofsäss, H., Zhang, K., & Mutzke, A. 2014, Simulation of Ion Beam Sputtering with SDTrimSP, TRIDYN and SRIM, *ApSS*, **310**, 134
- Johnson, R. E. 1990, in *Energetic Charged-Particle Interactions with Atmospheres and Surfaces*, ed. Johnson (1st ed.; Berlin: Springer)
- Johnson, R. E., & Brown, W. L. 1982, Electronic Mechanisms for Sputtering of Condensed-Gas Solids by Energetic Ions, *NIMPR*, **198**, 103
- Johnson, R. E., Lanzerotti, L. J., & Brown, W. L. 1984, Sputtering Processes: Erosion and Chemical Change, *AdSpr*, **4**, 41

- Killen, R. M., Morrissey, L. S., Burger, M. H., et al. 2022, The Influence of Surface Binding Energy on Sputtering in Models of the Sodium Exosphere of Mercury, *PSJ*, **3**, 139
- Lavorenti, F., Jensen, E. A., Aizawa, S., et al. 2023, Maps of Solar Wind Plasma Precipitation onto Mercury's Surface: A Geographical Perspective, *PSJ*, **4**, 163
- Madey, Theodore E., Yakshinskiy, B. V., Ageev, V. N., & Johnson, R. E. 1998, Desorption of alkali atoms and ions from oxide surfaces: Relevance to origins of Na and K in atmospheres of Mercury and the Moon, *JGR*, **103**, 5873
- Martinez, R., Langlinay, T., Ponciano, C. R., et al. 2017, Sputtering of Sodium and Potassium from Nepheline: Secondary Ion Yields and Velocity Spectra, *NIMPB*, 406, 523
- Massetti, S., Mangano, V., Milillo, A., et al. 2017, Short-term Observations of Double-peaked Na Emission from Mercury's Exosphere, *GeoRL*, **44**, 2970
- McGrath, M. A., Johnson, R. E., & Lanzerotti, L. J. 1986, Sputtering of Sodium on the Planet Mercury, *Natur*, **323**, 694
- Morrissey, L. S., Bringuier, S., Bu, C., et al. 2024, Solar Wind Ion Sputtering from Airless Planetary Bodies: New Insights into the Surface Binding Energies for Elements in Plagioclase Feldspars, *PSJ*, **5**, 272
- Morrissey, L. S., Lewis, J., Ricketts, A., et al. 2025, Theoretical Calculations on the Effect of Adsorbed Atom Coverage on the Sodium Exospheres of Airless Bodies, *ApJ*, **981**, 73
- Morrissey, L. S., Schaible, M. J., Tucker, O. J., et al. 2023, Establishing a Best Practice for SDTrimSP Simulations of Solar Wind Ion Sputtering, *PSJ*, **4**, 67
- Morrissey, L. S., Tucker, O. J., Killen, R. M., Nakhla, S., & Savin, D. W. 2022, Solar Wind Ion Sputtering of Sodium from Silicates Using Molecular Dynamics Calculations of Surface Binding Energies, *ApJL*, **925**, L6
- Mutzke, A. G., Schneider, R., Eckstein, W., et al. 2019, SDTrimSP Version 6.00." (IPP 2019-02) (Garching: Max-Planck-Institut Für Plasmaphysik)
- Nittler, L. R., Starr, R. D., Weider, S. Z., et al. 2011, The Major-Element Composition of Mercury's Surface from MESSENGER X-Ray Spectrometry, *Sci*, **333**, 1847
- Nittler, L. R., & Weider, S. Z. 2019, The Surface Composition of Mercury, *Eleme*, **15**, 33
- Peplowski, P. N., Lawrence, D. J., Evans, L. G., et al. 2015, Constraints on the Abundance of Carbon in Near-Surface Materials on Mercury: Results from the MESSENGER Gamma-Ray Spectrometer, *P&SS*, **108**, 98
- Potter, A. E., Killen, R. M., & Morgan, T. H. 2002, The Sodium Tail of Mercury, *M&PS*, **37**, 1165
- Raines, J. M., Dewey, R. M., Staudacher, N. M., et al. 2022, Proton Precipitation in Mercury's Northern Magnetospheric Cusp, *JGRA*, **127**, 1
- Raines, J. M., Gershman, D. J., Slavin, J. A., et al. 2014, Structure and Dynamics of Mercury's Magnetospheric Cusp: MESSENGER Measurements of Protons and Planetary Ions, *JGRA*, **119**, 6587
- Sarantos, M., Killen, R. M., Surjalal Sharma, A., & Slavin, J. A. 2010, Sources of sodium in the lunar exosphere: Modeling using ground-based observations of sodium emission and spacecraft data of the plasma, *Icar*, **205**, 364
- Schmidt, C. A., Baumgardner, J., Mendillo, M., & Wilson, J. K. 2012, Escape Rates and Variability Constraints for High-Energy Sodium Sources at Mercury, *JGRA*, **117**, 1
- Sigmund, Peter 1969, Theory of Sputtering. I. Sputtering Yield of Amorphous and Polycrystalline Targets, *PhysRev*, **187**, 768
- Sigmund, P. 1981, Sputtering by Ion Bombardment Theoretical Concepts, in Sputtering by Particle Bombardment I, Topics in Applied Physics, ed. Behrisch, Vol. 47 (Berlin: Springer-Verlag), 9
- Sigmund, P. 2017, Six Decades of Atomic Collisions in Solids, *NIMPB*, **406**, 391
- Solomon, S. C., McNutt, R. L., Gold, R. E., & Domingue, D. L. 2007, MESSENGER Mission Overview, *SSRv*, **131**, 3
- Swordy, S. P. 2001, The Energy Spectra and Anisotropies of Cosmic Rays, *SSRv*, **99**, 85
- Szabo, P. S., Biber, H., Jäggi, N., et al. 2020, Experimental Insights Into Space Weathering of Phobos: Laboratory Investigation of Sputtering by Atomic and Molecular Planetary Ions, *JGRE*, **125**, 1
- von Steiger, R., Schwadron, N. A., Fisk, L. A., et al. 2000, Composition of quasi-stationary solar wind flows from Ulysses/Solar Wind Ion Composition Spectrometer, *JGR*, **105**, 27217
- Wiens, R. C., Burnett, D. S., Calaway, W. F., Hansen, C. S., Lykke, K. R., & Pellin, M. J. 1997, Sputtering Products of Sodium Sulfate: Implications for Io's Surface and for Sodium-Bearing Molecules in the Io Torus, *Icar*, **128**, 386
- Wurz, P., Fatemi, S., Galli, A., et al. 2022, Particles and Photons as Drivers for Particle Release from the Surfaces of the Moon and Mercury, *SSRv*, **218**, 10
- Yakshinskiy, B. V., & Madey, T. E. 2000, Desorption induced by electronic transitions of Na from SiO<sub>2</sub>: relevance to tenuous planetary atmospheres, *Surface Sci.*, **451**, 160
- Yakshinskiy, B. V., & Madey, T. E. 2005, Temperature-Dependent DIET of Alkalis from SiO<sub>2</sub> Films: Comparison with a Lunar Sample, *SurSc*, **593**, 202
- Ziegler, J. F., Ziegler, M. D., & Biersack, J. P. 2010, SRIM—The Stopping and Range of Ions in Matter, *NIMPB*, **268**, 1818
- Zhao, J.-T., Zong, Q.-G., Sun, W.-J., et al. 2024, Dynamics of Sputtered Neutral Sodium Atoms in the Near-Mercury Space, *JGRA*, **129**, e2023JA032139